Selective focusing through target identification and experimental acoustic signature extraction: Through-aberration experiments

Ali Mcheik, Garance Sauderais, Adrien Arnaud, Samuel Rodriguez

Ultrasonics 151 (2025) 107605

Contents lists available at ScienceDirect

Ultrasonics

journal homepage: www.elsevier.com/locate/ultras

Selective focusing through target identification and experimental acoustic signature extraction: Through-aberration experiments

Ali Mcheik, Garance Sauderais[1], Adrien Arnaud, Samuel Rodriguez *

University of Bordeaux, CNRS, Bordeaux INP, I2M, UMR 5295, F-33400, Talence, France

ARTICLE INFO

Keywords:
Wave focusing
Topological imaging
Inverse filtering
Phase aberration
Focused ultrasound

ABSTRACT

In the first part of this work (Rodriguez et al. 2016), the selective focusing through identification and experimental acoustic signature extraction (SelF-EASE) method was presented, and its potential for accurate ultrasound focusing was assessed via numerical experiments. In the second part of this work, the inversion procedure and focusing signal extraction are improved in terms of reliability and computation time, and experimental results are presented. First, the improved signature extraction process is evaluated with two experimental aluminum samples. Second, the improved focusing process is experimentally performed on a target immersed in water behind an unknown aberration layer. Compared with the time-of-flight methods, the measured intensity fields greatly improve in terms of accuracy without any further knowledge of the medium.

1. Introduction

Space- and time-dependent controlled acoustic fields are used in many applications, such as ultrasound imaging, high- and low-intensity medical applications, and contact-free object manipulation. Controlling the phase of a transducer array that generates waves in a large known homogeneous medium with appropriate delay laws addresses this need. Controlling this phase in a more complex medium requires more advanced techniques. The first approach that is used mainly in medical imaging is to correct the effects of aberrations without knowing or retrieving the inhomogeneity maps. Adaptative imaging introduces phase-aberration correction to retrieve the resolution and contrast that can be obtained in the absence of unknown aberrators. Multiple insonifications of the medium and a point-like scatterer used as a guide star [1] or a speckle-based target [2–4] are needed. Another concern of medical imaging is addressing the multiple scattering effects of weakly inhomogeneous media such as human soft tissues. Matricial imaging approaches [5] allow the separation of multiple scattering contributions from single scattering contributions in images obtained in a weakly inhomogeneous medium. In the distortion matrix approach [6], multiple scattering contributions are discarded, and the unknown aberration effects are corrected. An iterative focusing process can also be used to retrieve the local green functions, which allows for the correction of phase aberrations [7]. All these methods are used to enhance images, but the phase corrections obtained could also be used to generate more accurate focused beams in the inspected medium. In the previously cited methods, multiple insonifications are obtained either by firing each emitter successively or by generating multiple angle plane waves, and the coherent information is extracted from a comparison between either the signals or the images obtained with these insonifications. SelF-EASE relies on another approach that can extract a target signature with a single insonification. In the first set of experimental results in the present study, a small scatterer is selected as the target. However, previous numerical experiments have demonstrated that a virtual target can also be added anywhere in an image [8].

The second approach for generating controlled beams in a complex medium is to take advantage of advanced knowledge of the medium. For example, knowing the experimental radiation pattern of transducers in a complex medium allows the synthesis of a controlled acoustic field [9]. For transcranial applications, measuring the computed tomography (CT) scans of the skull allows the aberration corrections to be computed [10,11]. If the aberrating objects are disregarded, the homogeneity hypothesis will lead to distorted images and to a deviation of the focal spot to an undesired location. In the following experimental application of SelF-EASE, this advanced knowledge about the medium is not necessary. In the case of even stronger aberrators, however, its theoretical framework can take into account this knowledge [12].

The third approach to correct the aberrations involves the use of a field monitoring device that indicates where the focusing occurs and then to correct the delay laws for recalibration. For high-intensity focusing ultrasound (HIFU) thermoablation techniques, magnetic resonance

* Corresponding author.
E-mail address: samuel.rodriguez@u-bordeaux.fr (S. Rodriguez).
[1] Present address: SATIE - UMR CNRS 8029, CY Cergy-Paris Université, France.

https://doi.org/10.1016/j.ultras.2025.107605
Received 20 July 2024; Received in revised form 24 January 2025; Accepted 20 February 2025
Available online 1 March 2025

(MR) guidance allows temperature monitoring [13] and the movement of the probe to the desired location or the correction of delay laws [14]. Another acoustic device can also be used to track HIFU ablation [15] or cavitation [16]. Ultrasound-induced neurostimulation requires a lower pressure level, as damage is prohibited. MR thermography can thus no longer be used. Electroencephalography (EEG) and functional magnetic resonance imaging (MRI) are used instead to monitor brain activity [17]. To treat kidney stones, the focus of the lithotripter is aligned via either ultrasonic imaging or X-ray fluoroscopy [18]. The drug delivery allowed by the reversible blood–brain barrier permeabilization [19,20] and the development of transcranial vortices focusing for contact-free manipulation [11] also motivate the development of accurate focusing methods behind aberrating layers such as the skull. Ribs are also a natural obstacle for HiFU treatment [21]. The long-term ambition of SelF-EASE is to be free of the need for outer guidance, such as MRI, ultrasound or X-ray.

First, the main steps of the method are summarized, and the improvements made since the first paper [8] are detailed. Two sets of experiments are presented. The first set of experiments, which includes simple drilled aluminum samples, allow us to understand how to use the new inversion tools developed and to demonstrate the efficiency of the acoustic signature process in the presence of nonnegligible local multiple scattering. The second set of experiments, which involves a single target located behind an aberrating medium, is aimed at showing how the method can achieve accurate focusing without any knowledge of the aberrating layer. These results are supported by wave field measurements.

2. SelF-EASE methodology

2.1. Summary of the methods

The experimental acoustic signature extraction (EASE) method can be summarized in four steps. First, the medium is classically investigated using a transducer array that emits waves and measures the response of the medium. Second, an image of the medium is computed based on the previously obtained experimental data. Third, the image is modified in such a way that only the identified focalization targets remain in the image. Fourth, the inverse imaging procedure converts the modified image into the signals associated with the target(s). The imaging method chosen is topological imaging [22–24]. The fast topological imaging method (FTIM) [25] complies with a matrix formalism [8], making the inverse imaging procedure a one-step procedure. When a semi-infinite homogeneous reference medium and ray-tracing propagation model are assumed for computing an image, the FTIM is equivalent to the classical delay and sum method [12]. Nevertheless, FTIM formalism allows easy separation of emission and reception signals and is more general, as it is compatible with more complex reference media, such as heterogeneous [12], anisotropic [26], reverberating [27,28] media or wave guides [29].

In [8], the imaging function at pixel location $\mathbf{M}$ is given by $|G(\mathbf{M})|$, where $G(\mathbf{M})$ is defined in the frequency domain with the following matrix formalism:

$$\mathbf{G} = A\mathbf{X} \tag{1}$$

knowing that

$$G_k = G(\mathbf{M}_k) \tag{2a}$$

$$X_l = \left(R_j(\omega_m) - U(\mathbf{M}_j, \omega_m)\right)^* \text{ with } l = (j-1)N_\omega + m \tag{2b}$$

$$A_{kl} = -H_j^r(\mathbf{M}_k, \omega_m) \sum_{i=1}^{N_e} H_i^e(\mathbf{M}_k, \omega_m) E_i(\omega_m) \tag{2c}$$

where $R_j(\omega_m)$ corresponds to the signal measured by the jth receiving transducer at angular frequency ω_m and where $U(\mathbf{M}_j, \omega_m)$ is the direct problem solution simulated in the reference medium at location $\mathbf{M}_j$ of the jth receiver. N_e corresponds to the number of emitting elements and * denotes complex conjugation. In our case, the reference medium is homogeneous and semi-infinite, and a plane wave is generated by an array composed of transducers used for both emission and reception. Thus, the difference $\left(R_j - U(\mathbf{M}_j)\right)$ corresponds to the sole signals measured R_j that are simply set to 0 during the emission duration. $H_j^r(\mathbf{M})$ and $H_i^e(\mathbf{M})$ correspond to the transfer functions between receiver j and point $\mathbf{M}$ and between emitter i and point $\mathbf{M}$, respectively. In our case, the same transducers are used for both emission and reception. Thus, $H_i(\mathbf{M})$ does not need to be distinguished between the emitter and the receiver. Finally, E_i corresponds to the emission signal transmitted by transducer i.

Matrix A is constructed of N_p rows and $N_\omega N_r$ columns, where N_p, N_ω and N_r are the numbers of pixels, angular frequency samples and receivers, respectively. Building image vector $\mathbf{G}$ is the second step of the EASE process. The third step of the EASE process consists of modifying the image so that it only includes the identified targets on which focusing is expected. The corresponding modified image is denoted $\mathbf{G}_{mod}(\mathbf{M})$. The final steps of the EASE process consist of an inversion procedure of Eq. (1), which yields $\mathbf{X}_{mod}$, the acoustic signature corresponding to $\mathbf{G}_{mod}$, *i.e.,* the acoustic signature of the target(s). The method can be interpreted as an inverse filtering technique [30], in which a desired ultrasonic image is retrieved instead of a desired wave field. A condition for successful application is that the target can be identified in the image (or at least the neighboring environment [8]). The main advantage is that no absolute position of the target is needed. Even if the image obtained is distorted and inaccurate in terms of space coordinates, the acoustic signature extracted should be correct. Backpropagating this signature will ensure accurate focusing. Another condition for successful application is that the same receiving transducers should be used for imaging and focusing. The emitters can still be different. Compared with [8], the inversion procedure has been improved, and a delay law computation method based on the extracted acoustic signature $\mathbf{X}_{mod}$ is proposed to take full advantage of the array width and to use any desired excitation signal for generation.

2.2. Improved image inversion process

The inversion problem is how to retrieve $\mathbf{X}_{mod}$ from Eq. (3).

$$\mathbf{G}_{mod} = A\mathbf{X}_{mod} \tag{3}$$

where A is a rectangular matrix. This corresponds to a least-squares minimization of

$$L(\mathbf{X}) = \|\mathbf{G}_{mod} - A\mathbf{X}\|_2^2 \tag{4}$$

An appropriate approach is to use generalized inverse matrices. Those based on Penrose conditions [31] are unique and easy to compute on the basis of singular value decomposition (SVD). Noting that A^+ is the Moore–Penrose inverse of A, the least-squares solutions of Eq. (3) are given by $A^+G_{mod} + (I - A^+A)w$ with any vector w. If matrix A is a full column rank matrix, then the pseudoinverse can be obtained without SVD decomposition as $A^+ = (A^*A)^{-1}A^*$, where A^* denotes the conjugate transpose. Furthermore, $A^+A = I$, and only one least-squares solution exists $X_{mod} = A^+G_{mod}$. This full column rank case is the only one considered in the first paper presenting SelF-EASE [8]. This is a quite restrictive assumption with two direct consequences. First, the number of rows N_p must be greater than the number of columns $N_\omega N_r$. In practice, this implies a large number of pixels. For example, the typical values encountered in the results presented in the last section are as follows: There are $N_r = 128$ transducers. The frequency bandwidth of interest is 1.125–3.375 MHz, and the acquisition duration is 160 µs. This leads to the number of frequency points $N_\omega = 360$. Thus, the matrix is constructed of 46080 columns and should have more rows, *i.e.,* more pixels. Second, a full column rank means that the imaging function is injective and thus that the physical size of the domain covered by the image must be larger in width and depth than the possible exploration distance, which is roughly half

the measurement duration times the assumed wave velocity. In the same example, this lower limit is 120 mm. Both elements contribute to the need for a very large matrix A, making the inversion process computationally expensive. In the general case where no constraint is applied to the rank of A, the number of least-squares solutions is infinite, but $\mathbf{X}_{mod} = A^{+}\mathbf{G}_{mod}$ corresponds to the minimum-norm solution. In our case, this corresponds to the physical solution of the inverse problem, as any added component to the extracted acoustic signature would be the signature of other objects even if they are outside of the imaging domain corresponding to A. This allows us to restrict the inversed image $\mathbf{G}_{mod}$ to the pixels inside the cropped region noted Ω_t. Noting $A_{|\Omega_t} = A(\mathbf{M} \in \Omega_t, \omega)$ the restriction of A to Ω_t and $\mathbf{G}_{mod|\Omega_t}$ the restriction of $\mathbf{G}_{mod}$ to Ω_t, the new inverse problem is as follows:

$$\mathbf{G}_{mod|\Omega_t} = A_{|\Omega_t}\mathbf{X}_{mod} \tag{5}$$

In practical use, this approach drastically reduces the number or rows of matrix A, accelerating the SVD decomposition of A and the computation of A^{+}. In the case of Section 3, the SVD of the matrix A takes 584 s, whereas that of matrix $A_{|\Omega_t}$ takes 1.67 s when the same CPU is used, which corresponds to a 350 speed-up factor.

The function to be minimized is now given by Eq. (6)

$$L_{\Omega_t}(\mathbf{X}) = \|\mathbf{G}_{mod|\Omega_t} - A_{|\Omega_t}\mathbf{X}\|_2^2 \tag{6}$$

The physical solution of this problem is given by Eq. (7).

$$\mathbf{X}_{mod} = A^{+}_{|\Omega_t}\mathbf{G}_{mod|\Omega_t} \tag{7}$$

Matrix $A^{+}_{|\Omega_t}$ is an $N'_p \times (N_\omega N_r)$ matrix with N'_p being the number of pixels in Ω_t. It is given by:

$$A^{+}_{|\Omega_t} = V S^{+} U^{*} \tag{8}$$

where U, S and V are given by the SVD of matrix $A_{|\Omega_t} = USV^{*}$. The matrix S is rectangular but has only nonzero values $\lambda_i = S_{ii}$ on its diagonal. These values correspond to the singular values. S^{+} is an $(N_\omega N_r) \times N'_p$ matrix, which has nonzero values only on its diagonal. Theoretically, these values are given by $1/\lambda_i$. In practice, the smallest singular values generate noise and make nonphysical results dominant after inversion. The singular values are thus filtered such that:

$$S^{+}_{ii} = \begin{cases} \dfrac{1}{\lambda_i} & \text{if } i \geq i_{max} \\ 0 & \text{if } i < i_{max} \end{cases} \tag{9}$$

Choosing an appropriate value for the filtering criterion i_{max} is critical for obtaining meaningful results. This criterion is equivalent to adding a regularization term to the cost function L_{Ω_t}, and an appropriate tool for determining the optimal criterion is plotting the L-curve [32]. Two L-curves can be defined in our case depending on the misfit function chosen: the local L-curve (Eq. (10)) or the global L-curve (Eq. (11)). As only the pseudoinverse of $A_{|\Omega_t}$ is computed, the only L-curve that makes sense for Hansen's and O'Leary's work corresponds to the local L-curve. The coordinates of the points of these curves are given by:

$$\left(\|\mathbf{X}_{mod}\|, \|L_{\Omega_t}(\mathbf{X}_{mod})\|\right) \text{ for the } local \text{ L-curve,} \tag{10}$$

$$\left(\|\mathbf{X}_{mod}\|, \|L_{\Omega}(\mathbf{X}_{mod})\|\right) \text{ for the } global \text{ L-curve.} \tag{11}$$

for all the possible cutoff indices i_{max}. [32] stated that the shape of the L-curve with logarithmic scales is expected to resemble the letter L and that the optimal choice for the regularization parameter (the truncation index of the singular values in our case) is expected to correspond to the corner of that L in what is here defined as the local L-curve. However, the first set of experiments demonstrates that this is not necessarily what makes physical sense in the EASE method.

2.3. Improved focusing process

After the EASE process, the extracted acoustic signature is used to generate a beam that focuses on the target. The strategy used in the first paper consists of using the time-reversed signature as emission signals. This allows broadband focusing, but the acoustic signature is prone to small magnitude signals for many transducers. Thus, the transducer array does not make use of its full power capabilities. Furthermore, if narrow band focusing is preferred, such as long-lasting quasimonochromatic emission, this is not possible. To address these limitations, the strategy used in this second part consists of extracting a delay law from the acoustic signature and using it as an advance law to be applied to any chosen synthesized excitation signal. In this publication, the delay law is obtained by unwrapping the phase of the Fourier transformed signature at a well-chosen angular frequency $\omega_d = 2\pi f_d$. For the `unwrap` function to be effective, the phase jump between two consecutive transducers must be smaller than π. This phase shift depends on the wave vector component parallel to the transducer array. The orientation of the wave vector stemming from the target depends on the target location relative to the array. Noting α_{max} the maximum possible angle between the wave vector and the vector normal to the array and noting p the array pitch, the maximal phase shift between two transducers is given by $\sin(\alpha_{\max})\frac{\omega}{C}p$. The condition for a successful application of `unwrap` is thus as follows:

$$f_d < \frac{C}{2p\sin(\alpha_{\max})} \tag{12}$$

This condition can also be interpreted as the spatial Shannon criterion, which states that there should be at least two transducers for one along-the-array projected wavelength $\frac{\lambda}{\sin(\alpha_{\max})}$. If this condition is fulfilled at ω_0, $\omega_d = \omega_0$. Otherwise, ω_d is chosen as the highest possible angular frequency verifying Eq. (12).

The phase shift $\phi_j(\omega_d) - \phi_i(\omega_d)$ between receiver i and receiver j is directly related to the time delay Δt_{ij} between them following Eq. (13).

$$\Delta t_{ij} = -\frac{\phi_j(\omega_d) - \phi_i(\omega_d)}{\omega_d} \tag{13}$$

Δt_{ij_0} is computed for every receiver i, and j_0 is chosen as the transducer with the most energetic signal for signal-to-noise ratio purposes. Using $\Delta t_{ij_0} - min(\Delta t_{ij_0})$ as an advance law for any chosen excitation signal is expected to generate a wave field that focuses on the target.

3. Experimental acoustic signature extraction application on aluminum samples

The classical singular value truncation methods are not well suited for our application. Pseudoinverse computation functions such as `pinv` in matlab[2] are based on the SVD decomposition of matrix A and a singular value truncation tolerance factor defined as $\epsilon(\max(\lambda_i)) * \max(\text{size}(A))$ where $\epsilon(x)$ returns the positive distance from $|x|$ to the next larger floating-point number of the same precision as x. It thus depends on the data type of x, typically single or double precision floats and only takes the numerical accuracy of the data type into account. L-curves and the associated truncation methods were developed in order to also take into account the presence of measurement noise superimposed to the true signal. In our case, this signal corresponds to the modified image. It is not only polluted with noise, it is also multiplied by a 0–1 weighting function defined by the user when cropping the target. For this reason, a specific singular value truncation method is here necessary for a meaningful image inversion. The experimental cases of this section are chosen to explain how to use L-curves in a way allowing appropriate singular value truncation and to demonstrate the efficiency of the EASE method.

[2] https://se.mathworks.com/help/matlab/ref/pinv.html

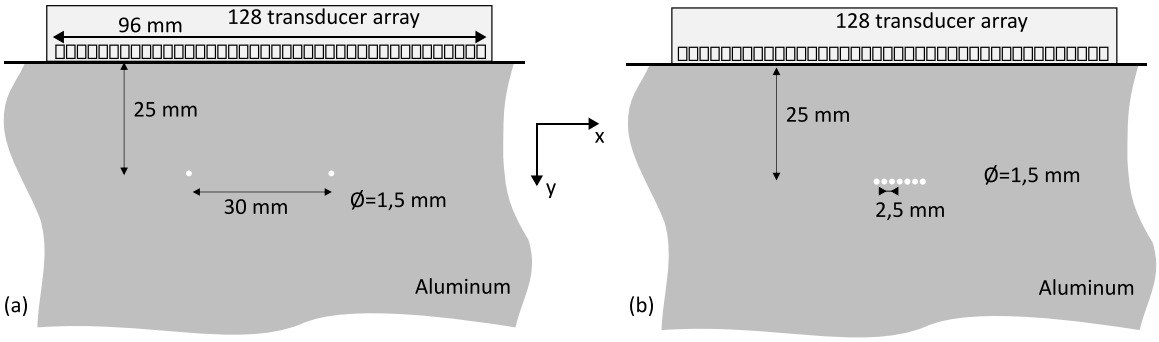

Fig. 1. Two aluminum samples under study and the corresponding experimental configurations: (a) two-hole sample and (b) seven-hole sample.

Both configurations described in Fig. 1 address known aluminum samples inspected with a 128-transducer 2.25 MHz Olympus 2.25L128-I3 array.[3] The pitch is 0.75 mm. The array is driven by a 128-channel TPAC (The Phased Array Company) Pioneer system.[4] Two distant holes are drilled in the first sample. Seven neighboring holes are drilled in the second sample. The in-between hole distances, 30 mm and 2.5 mm for configurations (a) and (b), respectively, are measured center to center. Similarly, the depth value of 25 mm is the distance between the upper side of the sample and the center of the drilled holes. A single normal quasiplane wave insonification is utilized. The quasiplane wave is obtained by firing all transducers simultaneously with the same burst signal defined with a three-period Gaussian time window.

The topological images are computed using a semi-infinite, 2D reference medium where only longitudinal waves can propagate. The velocity in the aluminum sample as well as the offset time of the array are estimated measuring two successive back and forth propagation between the array and the end of the sample knowing that the sample is 100 mm thick. The offset time of the array is 1.064 μs and the wave velocity in the sample is 6394 m/s. The radiation pattern of each element is obtained with a Rayleigh integral [33].

3.1. Two-hole case

The distant two-hole configuration makes it easy to identify the acoustic signatures of each hole when examining the raw signals shown in Fig. 2a. This is the first comprehensive test case. The corresponding topological image is shown in Fig. 2b. The two holes are clearly distinguished, and their locations correspond to those of the upper side of the drilled holes. The left hole is chosen as the target, and all the remaining pixels are set to 0. The corresponding modified image is shown in Fig. 2c. On the basis of the SVD of matrix $A_{|\Omega_t}$, the two L-curves are computed and presented in Fig. 2d. The local L-curve does not resemble the expected L-shape, and both curves present minima where the cost functions are thus minimized. These minima correspond to $i_{max} = 33$ and $i_{max} = 76$, respectively. The corresponding signatures obtained using these values are shown in Fig. 3a and 3b. Both extracted signatures are similar, and the efficiency of the process is evaluated by subtracting these signatures from the original raw signals, as shown in Fig. 3c,d. These subfigures are compared with the original raw signals of Fig. 2a. The signals corresponding to the left hole nearly completely vanish when the difference is obtained. This finding demonstrates that the acoustic signature extracted with the improved EASE process is accurate in terms of phase and magnitude for all the frequency content. In this simple case, choosing to minimize the local or global cost function in the extraction is not consequential. The next step is to perform extraction when the signature of the targeted object is mixed with other object signatures.

3.2. Seven-hole case

In the second test sample, the holes are closer to each other. The consequence is that the signatures of the holes are superimposed in the raw signals shown in Fig. 4a. Nevertheless, the resolution is sufficient for the holes to be distinguished in the image Fig. 4b. The second hole starting from the left is chosen as the target of the extraction process. The user crops the image to keep only the target as exposed in Fig. 4c. To perform the inversion properly, the two L-curves are computed and shown in Fig. 4d. Both L-curves present a local minimum similar to the two-hole case. However, a strong curvature point is also present on the local L-curve, which is more consistent with the expected corner of the L-shape. The corresponding signatures are computed and shown in Fig. 5. In contrast to the two-hole case, the extracted signatures here are quite different. The signature shown in Fig. 5a is qualitatively consistent with the expected signature of a relatively small object insonificated with a plane wave. To provide a physical interpretation of these signatures, the corresponding topological images are computed. The image shown in Fig. 5d is very similar to the cropped image in terms of location, magnitude and shape and confirms that the signature extracted on the basis of the minimization of the global cost function corresponds to the targeted second hole. The signature shown in Fig. 5b presents unexpected variations compared with the expected signature of a small object. The corresponding image (Fig. 5e) still shows agreement with the cropped image, but the spot corresponding to the target tends to be wider than the original spot and thus is not as reliable as Fig. 5d. The image shown in Fig. 5f, however, shows that the extracted signature corresponds not only to the sole second hole but also to the two neighboring holes, i.e., the first and third holes. Our interpretation is that in the original image, although the holes are resolved, the signature of their in-between interaction is superimposed with their own single-scattering signature. In other words, the acoustic interaction between these closed scatterers cannot be fully disregarded in comparison with their single contribution. Thus, the shape of the cropped image also contains information about the interaction of the target with its closed environment, which can be explained only by the presence of two neighboring scatterers. This is the information naturally retrieved in the signature of Fig. 5c corresponding to the inversion based on the cropped pixels only. The authors suggest that this result shows that the method has some potential for separating direct information from multiply scattered information. Nevertheless, this is beyond the scope of this paper, and the relevant signals for the selective focusing application are those retrieved when minimizing the global cost function (Fig. 5a), which forces the pixels next to the target to be set to zero and thus efficiently isolates the target.

We found from the first set of experiments that the inversion can be performed with the local imaging matrix restricted to the target region but that the singular value truncation index should be chosen to minimize the global cost function.

[3] https://www.olympus-ims.com/en/probes/immersion/
[4] https://thephasedarraycompany.com/product/pioneer/

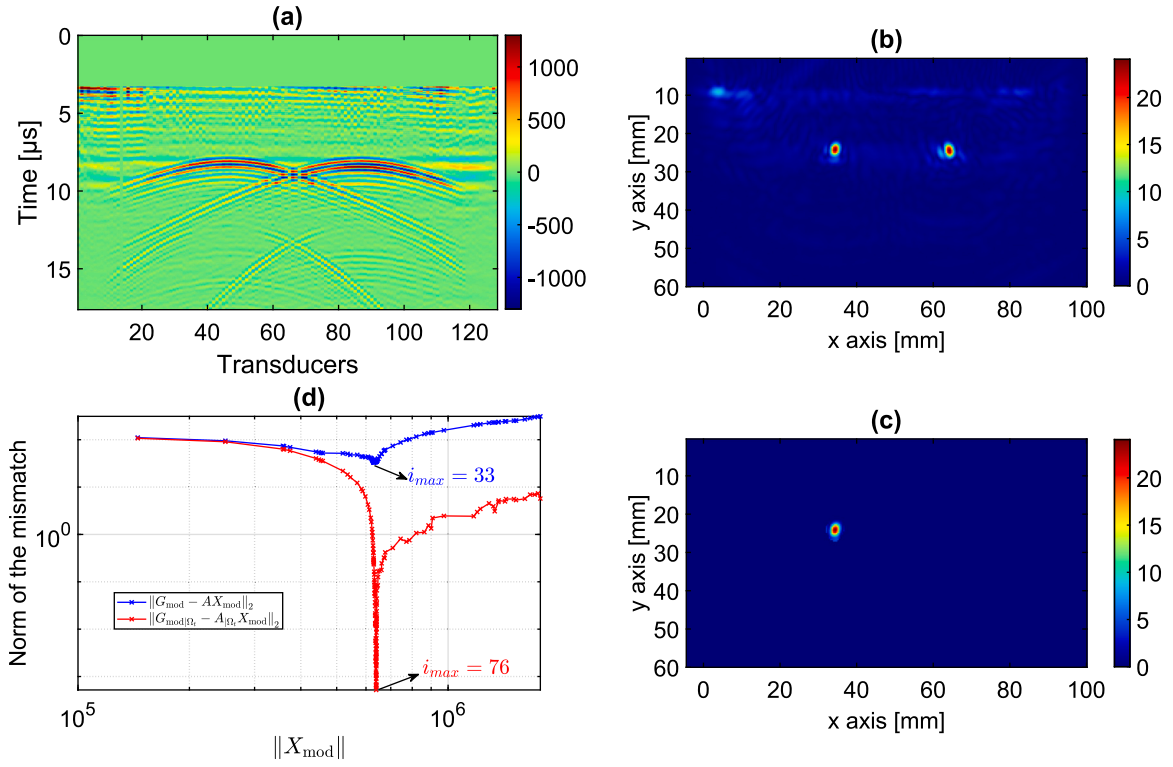

Fig. 2. Application of the EASE process to the 2-hole configuration-Part 1: (a) Raw acoustic signals (corresponding to vector **X**) after a single plane wave insonification; (b) topological image obtained (corresponding to vector **G**); (c) modified image after target selection (corresponding to $\mathbf{G}_{mod}$); and (d) local (Eq. (10)) and global (Eq. (11)) L-curves.

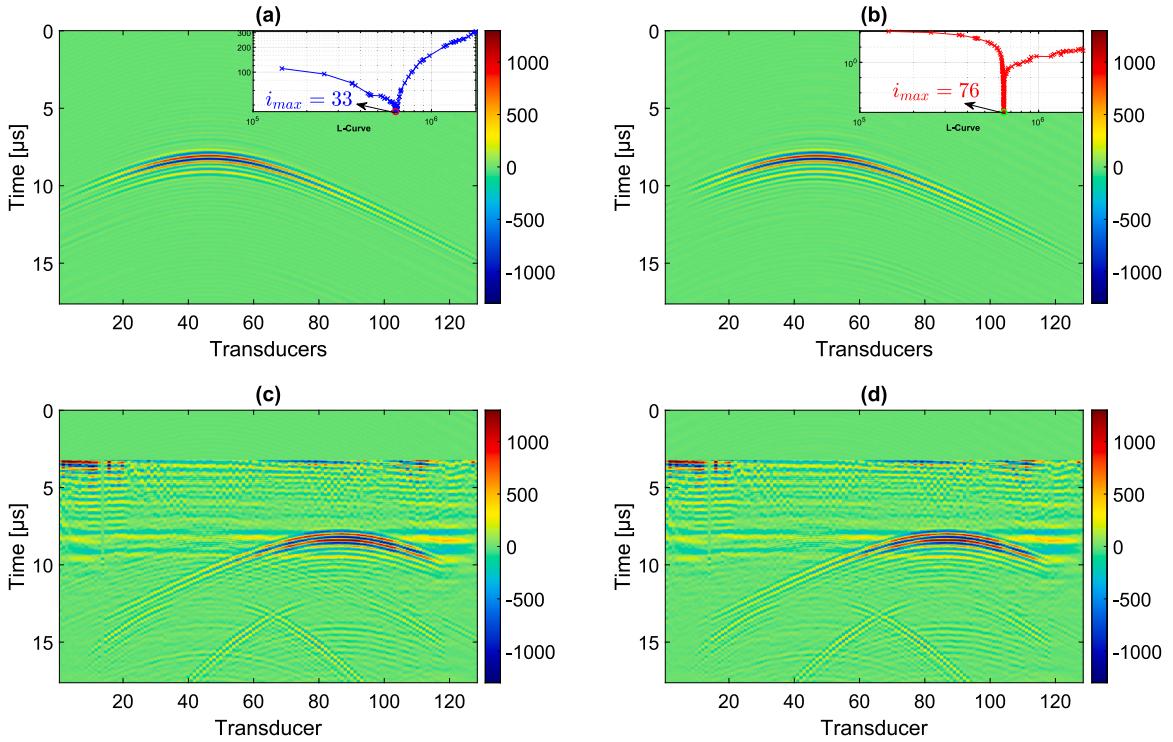

Fig. 3. Application of the EASE process to the 2-hole configuration-Part 2: (a) Extracted acoustic signature ($\mathbf{X}_{mod}$) based on the minimization of the local L-curve; (b) extracted acoustic signature ($\mathbf{X}_{mod}$) based on the minimization of the global L-curve; (c) difference between the raw experimental signals and the extracted signature of a single hole on the basis of the local L-curve; and (d) difference between the raw experimental signals and the extracted signature of a single hole on the basis of the global L-curve.

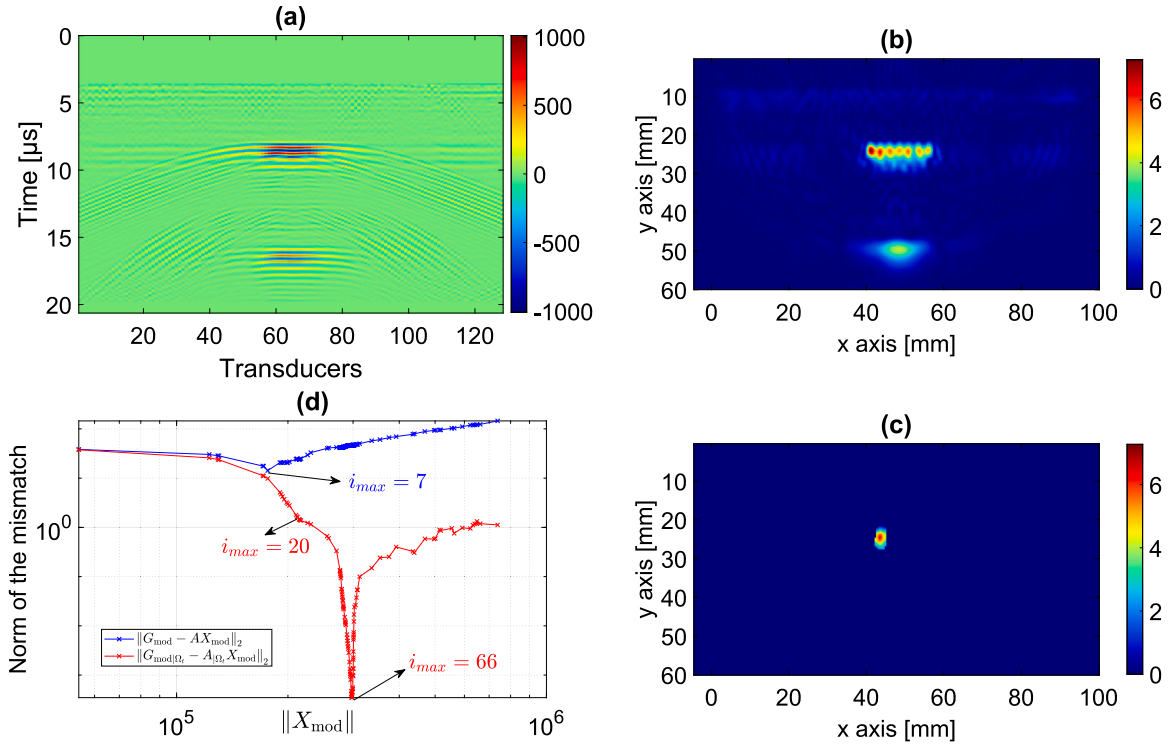

Fig. 4. Application of the EASE process to the 7-hole configuration-Part 1: (a) Raw acoustic signals (corresponding to vector **X**) after a single plane wave insonification; (b) topological image obtained (corresponding to vector **G**); (c) modified image after target selection (corresponding to $\mathbf{G}_{mod}$); (d) local (Eq. (10)) and global (Eq. (11)) L-curves.

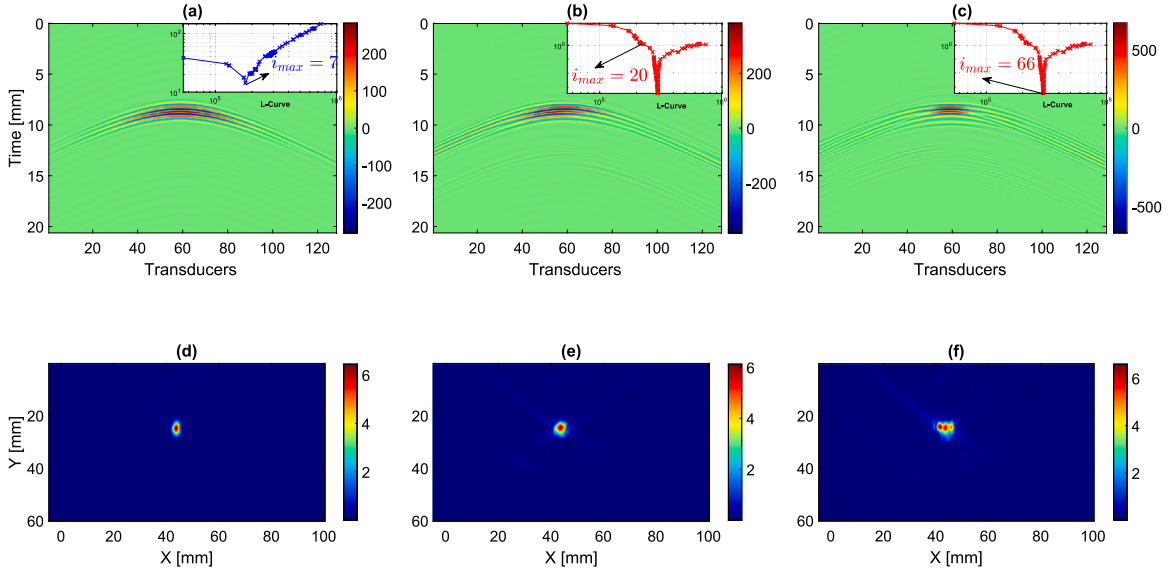

Fig. 5. Application of the EASE process to the 7-hole configuration-Part 2: (a) Extracted acoustic signature based on the minimization of the global L-curve; (b) extracted acoustic signature based on the inflection point of the local L-curve; (c) extracted acoustic signature based on the minimization of the local L-curve; and (d, e, and f) recomputed images based on the signatures of the subfigures (a, b, and c).

4. Experimental acoustic signature extraction and focusing application through an immersed aberrating interface

In the second set of experiments, the same 128-transducer array is immersed in water. This experiment is aimed at evaluating the accuracy of SelF-EASE in the presence of an unknown aberrator located between the array and the target, as presented in Fig. 6. The aberration layer is a plain, 3D-printed hexahedron composed of formlabs 10K[5] resin. The Young's modulus is typically 10 GPa, and the density is 2400 kg/m^3. The aberrating layer is made in such a way that it is invariant in the z direction and sufficiently large (125 mm) to be in accordance with the 2D propagation assumption. It is also 125 mm large in the x

[5] https://formlabs-media.formlabs.com/datasheets/2001479-TDS-FR-0.pdf

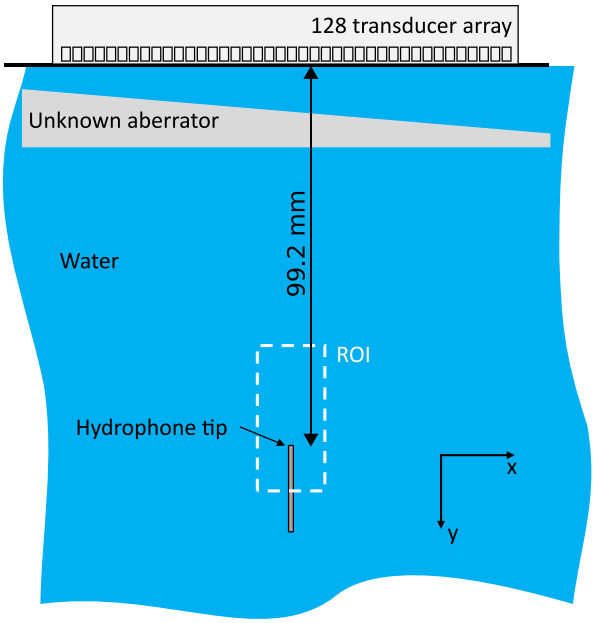

Fig. 6. Scheme of the experimental apparatus.

direction and is thus larger than the transducer array. Its thickness in the y direction varies linearly from 2.2 mm to 12.2 mm. This layer was designed as a first trial medium to test the method in a case where the effect of the aberration is relatively easy to understand. It is designed to have mechanical and thickness properties comparable to those of a skull but with a much simpler shape that does not break the 2D assumption and with a simpler structure as it is homogeneous over the thickness. It is meant as a first step that is not as simple as a constant-thickness layer. The method is evaluated by scanning the acoustic fields with a hydrophone. To know with great accuracy the initial location of the target, the tip of the unplugged hydrophone is used as the target.

The EASE process is applied on the basis of single quasiplane wave insonification and is shown in Fig. 7. The raw signals received are dominated by multiple echoes at the interfaces of the aberrating layer and water (Fig. 7a). The corresponding topological image is presented with a saturated color scale (Fig. 7b) to identify the targeted object, i.e., the tip of the hydrophone. The shape of the signature of the target of the image is distorted by the aberration layer but can still be identified. A zoom on the target signature is shown in subfigure Fig. 7c. In the absence of the aberrating layer, the shape of this signature is expected to be similar to those obtained in the aluminum samples, it is to say to be circular. The presence of the aberrating layer distorts here this signature into a bow shape. The cropped image (Fig. 7c) allows signature extraction (Fig. 7d) via the method defined in Section 3 using the pseudoinverse of $A_{|\Omega_t}$ and the cutoff singular value selection on the basis of the global L-curve.

A delay law is then extrapolated from the corresponding signature following the methodology described in Section 2.3. In the present configuration, the central frequency does not verify Eq. (12). The highest complying frequency is $f_d = 2.035$ MHz and is used for delay law computation. The delay law is transformed into an advance law referred as the SelF-EASE advance law. Two geometrical advance laws are also computed. They are all plotted in Fig. 8. The geometrical advance laws are computed based on the known velocity in water and the estimated distances between each transducer and the target. The first geometrical advance law is obtained using the exact location of the target with respect to the array. The second geometrical law is obtained using the location of the target in the image Fig. 7b. This location is inexact, as the image is based on a plain water assumption and is thus distorted by the aberrating layer but one could hope for a focusing accuracy improvement. The advance laws are applied to a synthesized three-period burst with a central frequency of 2.25 MHz that corresponds to a $\lambda_0 = 0.66$ mm wavelength. The generated 2D pressure fields are then measured in the vicinity of the initial location of the target (ROI in Fig. 6). The pulse intensity integral (PII) [34] is then computed based on the experimental pressure. The corresponding results are presented in Fig. 9 for evaluating the performances of the different advance laws.

The exact initial location of the hydrophone tip (when used as a passive target) relative to the array is acoustically measured before introducing the aberrator. This location corresponds to the coordinate $(0, 0)$ in the field measurements and is symbolized at scale 1 by a white line. All field measurements are performed with a 0.15 mm spatial step. The hydrophone diameter is 0.5 mm.

Using SelF-EASE (Fig. 9d), the focusing maximum is located at coordinates $(0, -0.3)$, which is near the exact location $(0, 0)$ of the target. The lateral accuracy is excellent. The longitudinal accuracy is very good, as the error corresponds to only 2.1% of the longitudinal size of the focusing spot. This result is compared to three other focusing attempts, one attempt in the absence of the aberrating layer (Fig. 9a) and two attempts in its presence (Fig. 9b-c). In the absence of the layer (Fig. 9(a)), the geometrical delay law #1 is applied and the magnitude maximum is located at $(0.15, 0.15)$, which is fairly accurate, as 0.15 mm is the spatial step of the field measurement. Using the same delay law in the presence of the layer (Fig. 9b) leads to focusing failure. The field maximum is located at $(3.9, -12.5)$, which is approximately 20 λ_0 away from the target. The higher wave velocity in the aberrating layer and its shape are responsible for a lateral deviation of the beam to the right and a convergent lens effect that moves the focusing point in the direction of the transducer array. The PII field corresponding to the geometrical delay law #2 is shown in Fig. 9c. The focusing point is located at $(-0.75, -16.5)$. A comparison with Fig. 9(b) shows that the lateral deviation is reduced but that the longitudinal deviation is worse. Because the higher velocity in the layer is disregarded in the image process, so the target appears closer to the array than it actually is. An analysis of Fig. 9(a-b) shows that the presence of the layer is also responsible for being closer to the array focusing point than the location that is used to compute the geometrical delay law. An initial conclusion of this set of measurements is that SelF-EASE allows accurate focus on the target in the presence of an aberration layer, contrary to geometrical advance laws, although both methods do not consider the presence of the layer. The key point for a successful application of EASE is to identify the target.

Comparing Fig. 9a and d, the focusing point maximal PII value is decreased by a factor of 6.24 due to the presence of the layer. This corresponds to a 2.50 decrease in pressure, which is attributed to the transmission effect at the interfaces and to the absorption in the resin of the aberrating layer. The sizes of the focusing spots are taken as the width of the spot at half the maximal magnitude. The longitudinal extents of the focusing spots are 10.2 mm and 14 mm for subfigures Fig. 9a and d respectively. The lateral extents are 1.00 mm and 1.14 mm. This corresponds to an increase in the size of the focusing spot of 37% in the longitudinal direction and 14% in the lateral direction. This set of measurements shows that the size increase of the focusing spot due to the aberration layer is not fully avoided by the method.

The present study successively deals with an aberrating layer which thickness typically corresponds to 10 wavelengths in surrounding water. The mechanical impedance mismatch is comparable to that of a water-bone interface. The plane surfaces and the plain 3D printing method tend to generate several high magnitude reflections, which pollute the image. The authors believe that an uneven and more attenuating layer such as a skull should generate less reflection artifacts. However, the tridimensional shape of biological interfaces may distort the wave propagation in a way that the target is poorly insonificated or that the target cannot be identified in the surrounding environment.

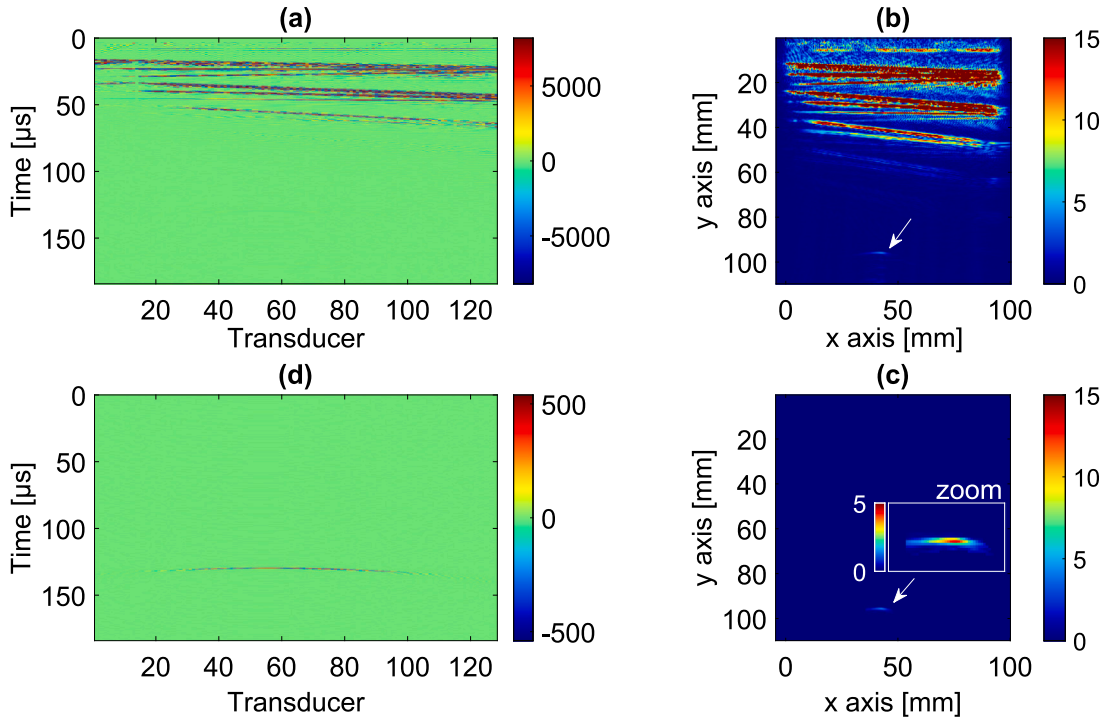

Fig. 7. Application of the EASE process to the target behind an aberrating interface: (a) Raw acoustic signals after a single plane wave insonification, (b) corresponding topological image with an arrow indicating the target, (c) cropped image after target selection, and (d) extracted signature of the target.

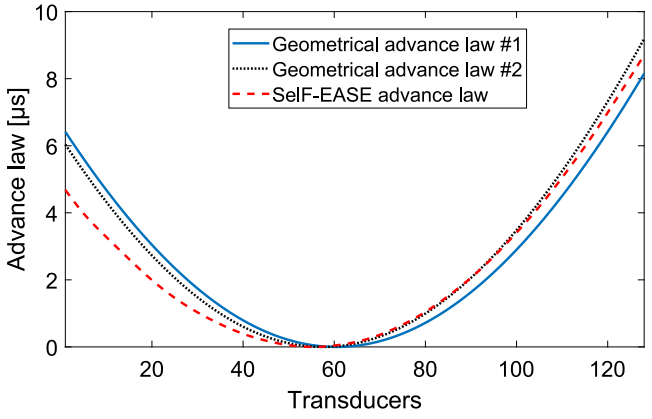

Fig. 8. The three tested advance laws.

It is thus not yet possible to say that the method will work as such whatever the aberrating layer. However, the authors believe that using several insonifications and aberration corrections should allow to extend the SelF-EASE method to biological environments.

5. Conclusions and perspectives

In the present paper, two methodological improvements of the SelF-EASE method are proposed, and two sets of experiments demonstrate its efficiency. The first improvement consists of a quicker inversion process that makes real-time implementation possible in the near future. The first set of experiments demonstrates the performance of the signature extraction process on a simple case and allows the best choice for the penalization criterion used in the inversion process to be defined. In a single-step procedure, the broadband acoustic signature of the in-the-image designated target is extracted even if local multiple scattering is present. The second set of experiments demonstrates that in a medium with an unknown aberration layer, the signature extraction process is also efficient. Moreover, the second methodological improvement, which consists of a delay law extraction procedure from the target signature, is successfully performed. The generated pressure field is measured in the vicinity of the initial target location. In these experiments, SelF-EASE allows the generation of a focusing spot localized on the target within a 2% error compared with the focusing spot dimensions. This result is compared with classical geometrical advance law computations based on two different target locations relative to the array: the exact location and the inexact location measured in the ultrasonic image computed with the aberration layer. In both cases, the focusing spot location error is between 75 and 300%, depending on the direction. These results experimentally demonstrate the focusing capabilities of SelF-EASE in the presence of an unknown aberrating medium even when a single insonification is used. There are two necessary conditions for its successful application. First, the target must be identified in the image by the user (or a program). Second, the array used for focusing must be the one used for receiving the signals in the image procedure.

The authors believe that there are numerous perspectives to this work, both for the methodology of SelF-EASE and for medical or other applications. On the methodological side, the next step involves the use of multiple insonifications to enhance the image signal-to-noise ratio and the target identification capabilities, eventually via adaptive imaging approaches. Another objective is to achieve real-time inversion. In the presence of an aberrating layer, the image of the medium could also be improved by integrating an approximation of the layer geometry based on an acoustic layer shape measurement. Notably, the known heterogeneity of the medium is considered in topological imaging. Another perspective numerically assessed in the first SelF-EASE publication is the addition of virtual targets to the image at locations chosen relative to the identified environment. This should also be confirmed experimentally. On the application side, high- or low-intensity focused medical applications could benefit from this technique, especially to reach areas behind aberrating media such as the skull or ribs. One long-term objective is to ensure accuracy so that third-party monitoring becomes unnecessary. Using functionalized,

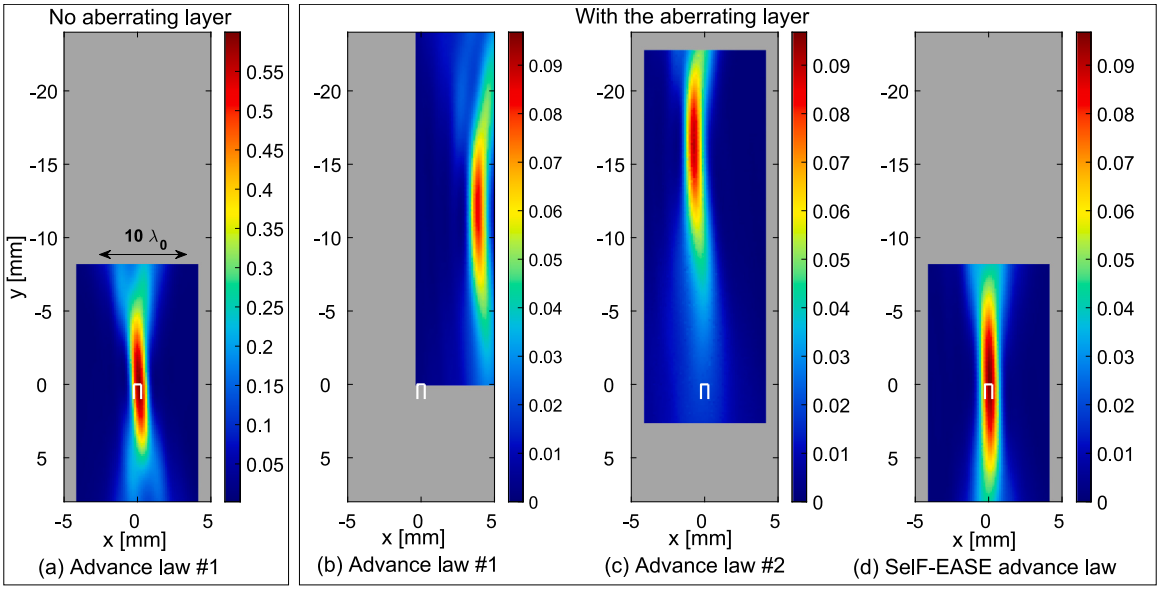

Fig. 9. PII (Pulse Intensity Integral) measured in the ROI in J.m^{-2} when applying the different advance laws: (a) in plain water using geometrical advance law #1 based on the exact location of the target; (b-d) in the presence of the aberrating layer, (b) using the same law as in (a), (c) using geometrical advance law #2 based on the relative location of the target in the image, and (d) using the advance law extracted from the signature of the target (whole enhanced SelF-EASE process). The real location of the hydrophone used first as the target is symbolized with white lines and is defined by coordinates (0, 0).

small, and highly echogenic objects such as contrast agents could also help targeting specific regions. We believe that this technique could also benefit some NDT applications, such as sonothermography, and contactless object manipulation methods, such as acoustic tweezers.

CRediT authorship contribution statement

Ali Mcheik: Visualization, Validation, Software, Methodology. **Garance Sauderais:** Software, Methodology. **Adrien Arnaud:** Software. **Samuel Rodriguez:** Writing – review & editing, Writing – original draft, Supervision, Software, Methodology, Conceptualization.

Declaration of competing interest

The authors declare that they have no known competing financial interests or personal relationships that could have appeared to influence the work reported in this paper.

Acknowledgments

We thank Enrico Panettieri (ENSAM-I2M) for printing the aberrating layer. We also thank Thomas Brunet (Bordeaux INP-I2M) for granting us access to the instrumented water tank in which the immersed experiments were performed. For the purpose of open access, a CC-BY public copyright license has been applied by the authors to the present document and will be applied to all subsequent versions up to the author accepted manuscript arising from this submission.

Data availability

The authors are unable or have chosen not to specify which data has been used.

References

[1] M. O'Donnell, S.W. Flax, Phase-aberration correction using signals from point reflectors and diffuse scatterers: Measurements, IEEE Trans. Ultrason. Ferroelectr. Freq. Control 35 (6) (1988) 768–774, http://dx.doi.org/10.1109/58.9334.

[2] M. Jaeger, E. Robinson, H.G. Akarçay, M. Frenz, Full correction for spatially distributed speed-of-sound in echo ultrasound based on measuring aberration delays via transmit beam steering, Phys. Med. Biol. 60 (11) (2015) 4497–4515, http://dx.doi.org/10.1088/0031-9155/60/11/4497.

[3] G. Chau, M. Jakovljevic, R. Lavarello, J. Dahl, A locally adaptive phase aberration correction (LAPAC) method for synthetic aperture sequences, Ultrason. Imaging 41 (1) (2019) 3–16, http://dx.doi.org/10.1177/0161734618796556.

[4] H. Bendjador, T. Deffieux, M. Tanter, The SVD beamformer: Physical principles and application to ultrafast adaptive ultrasound, IEEE Trans. Med. Imaging 39 (2019) 3100–3112.

[5] A. Aubry, A. Derode, Multiple scattering of ultrasound in weakly inhomogeneous media: Application to human soft tissues, J. Acoust. Soc. Am. 129 (1) (2011) 225–233, http://dx.doi.org/10.1121/1.3506343, arXiv:1003.1963, URL http://asa.scitation.org/doi/10.1121/1.3506343.

[6] W. Lambert, L.A. Cobus, T. Frappart, M. Fink, A. Aubry, Distortion matrix approach for ultrasound imaging of random scattering media, Proc. Natl. Acad. Sci. USA 117 (26) (2020) 14645–14656, http://dx.doi.org/10.1073/pnas.1921533117, arXiv:1912.05417.

[7] G. Montaldo, M. Tanter, M. Fink, Time reversal of speckle noise, Phys. Rev. Lett. 106 (5) (2011) http://dx.doi.org/10.1103/PhysRevLett.106.054301.

[8] S. Rodriguez, X. Jacob, V. Gibiat, Selective focusing through target identification and experimental acoustic signature extraction: Numerical experiments, Ultrasonics 68 (2016) 8–16, http://dx.doi.org/10.1016/j.ultras.2016.02.002, URL http://linkinghub.elsevier.com/retrieve/pii/S0041624X16000172.

[9] N. Quieffin, S. Catheline, R.K. Ing, M. Fink, Real-time focusing using an ultrasonic one channel time-reversal mirror coupled to a solid cavity, J. Acoust. Soc. Am. 115 (5) (2004) 1955, http://dx.doi.org/10.1121/1.1699396.

[10] J.F. Aubry, M. Tanter, M. Pernot, J.L. Thomas, M. Fink, Experimental demonstration of noninvasive transskull adaptive focusing based on prior computed tomography scans, J. Acoust. Soc. Am. 113 (1) (2003) 84–93, http://dx.doi.org/10.1121/1.1529663, arXiv:0402594v3, URL http://scitation.aip.org/content/asa/journal/jasa/113/1/10.1121/1.1529663.

[11] S. Jiménez-Gambín, N. Jiménez, F. Camarena, Transcranial focusing of ultrasonic vortices by acoustic holograms, Phys. Rev. Appl. 14 (5) (2020) 1, http://dx.doi.org/10.1103/PhysRevApplied.14.054070.

[12] H. Hafidi Alaoui, S. Rodriguez, M. Deschamps, Detection of defects in a 2D fluid-solid periodic cluster, Ultrasonics 112 (2020) (2021) 106307, http://dx.doi.org/10.1016/j.ultras.2020.106307.

[13] B. Quesson, M. Merle, M.O. Köhler, C. Mougenot, S. Roujol, B.D. De Senneville, C.T. Moonen, A method for MRI guidance of intercostal high intensity focused ultrasound ablation in the liver, Med. Phys. 37 (6) (2010) 2533–2540, http://dx.doi.org/10.1118/1.3413996.

[14] B.D. De Senneville, C. Mougenot, C.T. Moonen, Real-time adaptive methods for treatment of mobile organs by MRI-controlled high-intensity focused ultrasound, Magn. Reson. Med. 57 (2) (2007) 319–330, http://dx.doi.org/10.1002/mrm.21124.

[15] A. Battais, V. Barrère, W.A. N'Djin, A. Dupré, M. Rivoire, D. Melodelima, Fast and selective ablation of liver tumors by high-intensity focused ultrasound using a toroidal transducer guided by ultrasound imaging: The results of animal experiments, Ultrasound Med. Biol. 46 (12) (2020) 3286–3295, http://dx.doi.org/10.1016/j.ultrasmedbio.2020.08.001.

[16] C. Crake, S.T. Brinker, C.M. Coviello, M.S. Livingstone, N.J. McDannold, A dual-mode hemispherical sparse array for 3D passive acoustic mapping and skull localization within a clinical MRI guided focused ultrasound device, Phys. Med. Biol. 63 (6) (2018) http://dx.doi.org/10.1088/1361-6560/aab0aa.

[17] J. Blackmore, S. Shrivastava, J. Sallet, C.R. Butler, R.O. Cleveland, Ultrasound neuromodulation: A review of results, mechanisms and safety, Ultrasound Med. Biol. 45 (7) (2019) 1509–1536, http://dx.doi.org/10.1016/j.ultrasmedbio.2018.12.015.

[18] T.G. Leighton, R.O. Cleveland, Lithotripsy, Proc. Inst. Mech. Eng. Part H: J. Eng. Med. 224 (2) (2010) 317–342, http://dx.doi.org/10.1243/09544119JEIM588.

[19] K. Hynynen, N. McDannold, N.A. Sheikov, F.A. Jolesz, N. Vykhodtseva, Local and reversible blood–brain barrier disruption by noninvasive focused ultrasound at frequencies suitable for trans-skull sonications, NeuroImage 24 (1) (2005) 12–20, http://dx.doi.org/10.1016/j.neuroimage.2004.06.046.

[20] P. Mondou, S. Mériaux, F. Nageotte, J. Vappou, A. Novell, B. Larrat, State of the art on microbubble cavitation monitoring and feedback control for blood–brain-barrier opening using focused ultrasound, Phys. Med. Biol. 68 (18) (2023) http://dx.doi.org/10.1088/1361-6560/ace23e.

[21] E. Cochard, C. Prada, J.F. Aubry, M. Fink, Ultrasonic focusing through the ribs using the DORT method, Med. Phys. 36 (8) (2009) 3495–3503, http://dx.doi.org/10.1118/1.3159755, URL http://scitation.aip.org/content/aapm/journal/medphys/36/8/10.1118/1.3159755.

[22] B.B. Guzina, M. Bonnet, Topological derivative for the inverse scattering of elastic waves, Q. J. Mech. Appl. Math. 57 (2) (2004) 161–179, http://dx.doi.org/10.1093/qjmam/57.2.161.

[23] N. Dominguez, V. Gibiat, Y. Esquerre, Time domain topological gradient and time reversal analogy: an inverse method for ultrasonic target detection, Wave Motion 42 (1) (2005) 31–52, http://dx.doi.org/10.1016/j.wavemoti.2004.09.005.

[24] R. Tokmashev, A. Tixier, B.B. Guzina, Experimental validation of the topological sensitivity approach to elastic-wave imaging, Inverse Problems 29 (2013) 125005, http://dx.doi.org/10.1088/0266-5611/29/12/125005.

[25] S. Rodriguez, P. Sahuguet, V. Gibiat, X. Jacob, Fast topological imaging,, Ultrasonics 52 (8) (2012) 1010–1018, http://dx.doi.org/10.1016/j.ultras.2012.08.002.

[26] K. Metwally, E. Lubeigt, S. Rakotonarivo, J.F. Chaix, F. Baqué, G. Gobillot, S Mensah, Weld inspection by focused adjoint method, Ultrasonics 83 (2018) 80–87, http://dx.doi.org/10.1016/j.ultras.2017.08.009.

[27] S. Rodriguez, M. Veidt, M. Castaings, E. Ducasse, M. Deschamps, One channel defect imaging in a reverberating medium, Appl. Phys. Lett. 105 (24) (2014) 244107, http://dx.doi.org/10.1063/1.4904837, URL http://scitation.aip.org/content/aip/journal/apl/105/24/10.1063/1.4904837, http://aip.scitation.org/doi/10.1063/1.4904837.

[28] E. Lubeigt, S. Mensah, S. Rakotonarivo, J.-F. Chaix, F. Baqué, G. Gobillot, Topological imaging in bounded elastic media, Ultrasonics 76 (2017) 145–153, http://dx.doi.org/10.1016/j.ultras.2017.01.002, URL http://linkinghub.elsevier.com/retrieve/pii/S0041624X17300069.

[29] S. Rodriguez, M. Deschamps, M. Castaings, E. Ducasse, Guided wave topological imaging of isotropic plates, Ultrasonics 54 (7) (2014) 1880–1890, http://dx.doi.org/10.1016/j.ultras.2013.10.001.

[30] M. Tanter, J.L. Thomas, M. Fink, Time reversal and the inverse filter, J. Acoust. Soc. Am. 108 (1) (2000) 223–234, http://dx.doi.org/10.1121/1.429459, URL http://www.ncbi.nlm.nih.gov/pubmed/10923887.

[31] R. Penrose, A generalized inverse for matrices, Math. Proc. Cambridge Philos. Soc. 51 (3) (1955) 406–413, http://dx.doi.org/10.1017/S0305004100030401.

[32] P.C. Hansen, O. Prost, The use of the L-curve in the regularization of discrete ill-posed problems, SIAM J. Sci. Comput. 14 (6) (1993) 1487–1503.

[33] S. Rodriguez, Fast topological imaging software, 2024, URL https://github.com/samuelrodriguez2/Fast-Topological-Imaging-Software.git.

[34] T.L. Szabo, Diagnostic Ultrasound Imaging: Inside Out, second ed., Academic Press, Boston, 2014, http://dx.doi.org/10.1016/B978-0-12-396487-8.00018-5.